Unsteady load mitigation through a passive trailing-edge flap

Abel Arredondo-Galeana[a], Anna M. Young[b], Amanda S.M. Smyth[c], Ignazio Maria Viola[d,*]

[a]*Department of Naval Architecture, Ocean and Marine Engineering, University of Strathclyde, Glasgow, G4 0LZ, UK*
[b]*Department of Mechanical Engineering, University of Bath, Bath, BA2 7AY, UK*
[c]*Department of Engineering Science, University of Oxford, Oxford OX1 3PJ, UK*
[d]*School of Engineering, Institute for Energy Systems, University of Edinburgh, Edinburgh, EH10 4BY, UK*

Abstract

There are a wide range of applications in which it is desirable to mitigate unsteady load fluctuations while preserving mean loading. This is often achieved with active control systems, but passive systems are sometimes more desirable for enhancing reliability. This is the case, for example, for wind and tidal turbines, where unsteady loading limits the fatigue life of the turbine and results in power peaks at the generator. Here, we consider the unsteady load mitigation that can be achieved through a foil with a trailing-edge flap that is connected to the foil via a torsional spring. We develop a theoretical model and show that the preload can be tuned to preserve the mean foil loading. The spring moment that maximises the unsteady load mitigation is approximately constant, and the load fluctuation reduction is linearly proportional to the ratio of the flap to the full chord of the foil. We verify this relationship through water tunnel tests of a foil with a hinge at 25% of the chord from the trailing edge. As theoretically predicted, we measure unsteady load mitigation of up to 25%, without any variation in the mean load. In highly unsteady flow conditions, when boundary layer separation occurs, the unsteady load reduction decreases. Overall we conclude that passive trailing-edge flaps are effective in alleviating unsteady load fluctuations and their effectiveness depends on their size relative to the foil.

Keywords: unsteady aerodynamics; load alleviation; unsteady loading; passive trailing-edge flap; tidal energy

1. Introduction

In this paper we consider unsteady load mitigation on a foil with a passive trailing-edge flap, where the aim is to cancel the load fluctuations without affecting the mean load. This is relevant to a wide range of applications such as, for example, an aircraft flying in turbulence, and a yacht sailing in the atmospheric boundary layer. An application where mitigating load fluctuations is paramount for cost reductions is the tidal energy sector [1, 2, 3]. Technological developments have been introduced to reduce unsteady blade loading, such as passively bent-twist blades [4, 5]. However, such technology is limited to low frequency fluctuations and is not suitable for large

*Corresponding author
Email addresses: abel.arredondo-galeana@strath.ac.uk (Abel Arredondo-Galeana), Amy32@bath.ac.uk (Anna M. Young), amanda.smyth@eng.ox.ac.uk (Amanda S.M. Smyth), I.M.Viola@ed.ac.uk (Ignazio Maria Viola)

blades due to structural rigidity requirements. Active pitch control is another possible option, but this has an upper frequency limit due to the inertial effects of the blade [6]. Trailing-edge flaps, by contrast, can respond to higher frequencies better than the whole blade due to their smaller inertia [7, 8, 9, 10, 11].

Here, we consider how unsteady load mitigation can be achieved using a trailing-edge flap with a preloaded torsional spring at the hinge. The foil is set at a non-zero-lift angle of attack and is heaved sinusoidally in a uniform stream. We investigate the unsteady load mitigation for different frequencies and amplitudes of motion.

It is noted that the unsteady flow experienced by a heaving foil has similarities with that experienced by a turbine blade section due to a temporal change in the onset flow speed. A time-varying flow speed, which is uniform across the blade chord, can be due to a surface wave or a turbulent gust, for example. The chord of the outer blade sections, which are those most loaded, is almost parallel to the rotor plane. Hence, a change in the onset flow speed results in a change in the chord-normal flow velocity - a change that occurs simultaneously over the whole chord as in a heaving motion [1].

We will show through a theoretical model that unsteady load mitigation is possible without compromising the mean load. The theoretical model will also predict that the maximum unsteady load mitigation increases linearly from zero to 100%, as the hinge location is shifted from the trailing edge to the leading edge. We will test these hypotheses with water tunnel tests for one hinge location at 25% of the chord from the trailing edge, and confirm a 25% unsteady load reduction with no change to the mean loading. The unsteady effects are quantified through Theodorsen's linear theory and compared with experiments, revealing the range of validity of the theoretical model in terms of both the reduced frequency and the amplitude of the motion.

The manuscript is organised as follows. In §2, we describe the theoretical model for load alleviation of a foil with a passive trailing-edge flap. In §3, the experimental methodology is presented, including the two foils, the rig and the experimental set-up, and the kinematic parameters of the foil. Results are presented in §4. Specifically, the load measurements of both foils are presented in §4.1; the theoretically predicted loads are discussed in §4.2; the analysis of the measured and predicted deflections on the trailing edge flap are shown in §4.3; and flow diagnostics of the flow field are presented in §4.4 for the near wake. Concluding remarks are summarised in §5.

Interested readers can find additional analysis in the appendices. In §Appendix A we couple the unsteady model of the foil with a passive trailing-edge flap with a mass-spring-damper system and we show similar results to those from the unsteady model. In §Appendix B we present a step response test of the flap in the water tunnel where we obtain the dynamic parameters for the coupled model. In §Appendix C we present the phase averaged flowfields at four positions of the heaving kinematics. Finally, in Appendix D we show that, for a wind or a tidal turbine, velocity fluctuations due to the freestream velocity shear gradient are negligible, whilst changes in the angle of attack due to the same shear gradient are significant.

2. Theoretical model

This section describes the theoretical foundations of the load alleviation method proposed in this paper. The model considers a symmetric foil immersed in a uniform stream. At an angle of incidence, a symmetric foil that is free to pitch around its leading-edge would align itself to the incoming flow leading to zero lift force. Therefore, there must be some moment opposing the

pitching of the foil to allow lift generation. This constant moment, M_{k_s}, could be provided by a torsional spring, for example.

To formalise this concept, we consider the foil depicted in Fig. 1(a), which could represent a blade section in the rotor plane of a turbine. We refer to this as the equilibrium position. The foil is free to pitch at the leading-edge and has a mean angle of attack $\overline{\alpha}$, resultant flow velocity U, lift force L and a torsional spring moment M_{k_s} applied to the pitching axis. To ensure that the pitching foil provides the same lift as a rigid foil, the hydrodynamic pitching moment M_h must be equal and opposite to the moment provided by the spring: $M_{k_s} = -M_h$. For an ideal torsional spring, the moment increases linearly with the deformation, hence

$$M_{k_s} = k_s \theta_\mathrm{p}, \tag{1}$$

where θ_p is the spring preload angle. For a given M_h, a very flexible spring (very low k_s) needs to have a very high preload θ_p to ensure $M_{k_s} = -M_h$. For a rotation of the foil $\delta\theta$ that is small in comparison to the preload θ_p, the spring moment remains roughly constant. In fact,

$$M_{k_s} = k_s(\theta_\mathrm{p} \pm \delta\theta) \approx k_s \theta_\mathrm{p}. \tag{2}$$

This shows that, as mentioned above, a highly flexible foil (low k_s) has virtually a constant spring moment. From this observation, we notice that a highly flexible spring can be modelled numerically and experimentally by exerting a constant moment around the pitching axis.

Let us consider now an incremental change in the angle of attack $\delta\alpha$, while the flow velocity U remains unchanged. This scenario is depicted in Fig. 1(b). Using thin aerofoil theory, the increased angle of attack causes an increase in lift δL and an increase in the pitching moment δM_h:

$$\delta L = 2\pi\, \delta\alpha, \tag{3}$$

$$\delta M_h = \delta L\, x, \tag{4}$$

where x is the distance from the pitching axis of the foil (located at the leading-edge in this case) to the aerodynamic centre. This increase in hydrodynamic moment will generate a net moment and so the foil will re-pitch by $\delta\theta$ in the direction of the lift, as shown in Fig. 1(b). This will generate a further change in lift of

$$\delta L_2 = -2\pi\, \delta\theta. \tag{5}$$

From Eq. 2, the spring moment will not change, so once the foil is back in equilibrium,

$$M_{k_s} = -(M_h + \delta M_h) = -(M_h + 2\pi\, \delta\alpha\, x - \ 2\pi\, \delta\theta\, x). \tag{6}$$

Recalling that $M_{k_s} = -M_h$, this implies that

$$2\pi\, \delta\alpha\, x = 2\pi\, \delta\theta\, x, \tag{7}$$

and thus $\delta\alpha = \delta\theta$, and the load on the foil is unchanged (although the direction of the force has changed by $\delta\alpha$). This shows that maximum unsteady load cancellation is achieved by having a torsional spring which provides an approximately constant moment and when the entire foil pitches around an axis through the leading edge, load fluctuations can be entirely cancelled.

Let us now consider a flap with a chord length a attached to the foil by a torsional spring. Fig. 2(a) depicts the foil at its equilibrium condition for the mean angle of attack $\bar{\alpha}$. In the figure,

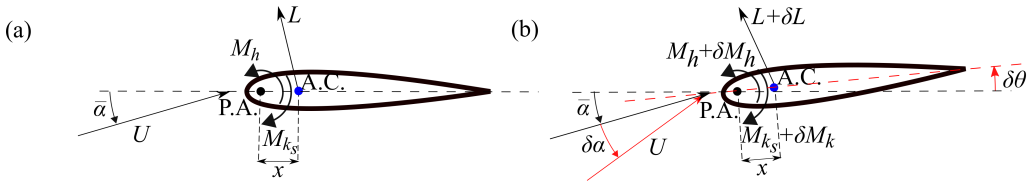

Figure 1: Foil pitching around the leading edge for (a) the mean flow condition and (b) an angle of attack increase of $\delta\alpha$ leading the foil to pitch by $\delta\theta$. In the figure, x is the distance from the pitching axis (P.A), located at the leading-edge, to the aerodynamic centre (A.C), located at 1/4 of the chord length.

the moments M_{k_s} and M_h balance each other and act on the pitching axis of the flap. The forces L and L_f are the lift forces on the front of the foil and on the flap, respectively. In Fig. 2(b), when a change $\delta\alpha$ in the angle of attack occurs, L on the front of the foil changes, while L_f remains constant because there can be no change in the moment about the spring and so the flap deflects in a similar manner to that described above for a foil rotating about its leading edge (Fig. 1).

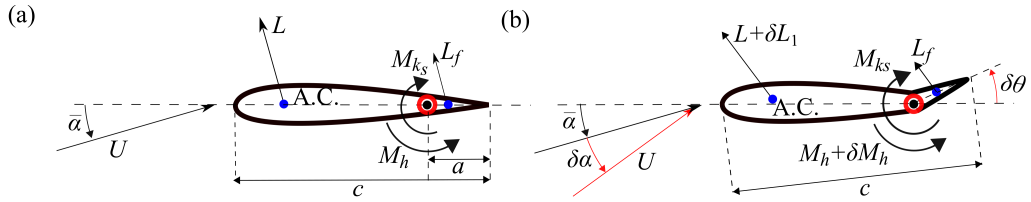

Figure 2: Foil with trailing-edge flap for (a) the mean flow condition and (b) an angle of attack increase of $\delta\alpha$ resulting in a flap deflection of $\delta\theta$.

Having introduced the concept of load alleviation by means of a pre-loaded spring attached to a freely pitching trailing-edge flap, a theoretical framework for the prediction of the associated load reduction will be presented in the following section.

2.1. Quasi-steady model

In the first instance, we use a linear, quasi-steady, panel method to estimate the load alleviation. We consider the rigid part of the foil and the flap as two separate panels. Each panel has a vortex of circulation Γ_n, which is located at $1/4$ the length of each panel, where n denotes the number of the panel. A collocation point cp_n is located at $3/4$ of the length of each panel. The equilibrium position is shown in Fig. 3(a). In the figure, x_p is the length of the first panel and a is the length of the second panel, r_{11} and r_{12} are the distances from the point where Γ_1 is applied to cp_1 and cp_2, and r_{21} and r_{22} the distances from the point where Γ_2 is applied to cp_1 and cp_2. The full chord is c. This model assumes small angle of attack oscillations. Hence, under these assumptions, the position of the vortex, collocation point and aerodynamic centre (A.C) in each panel remains constant. For larger angle of attack oscillations, we expect that this model will lose accuracy.

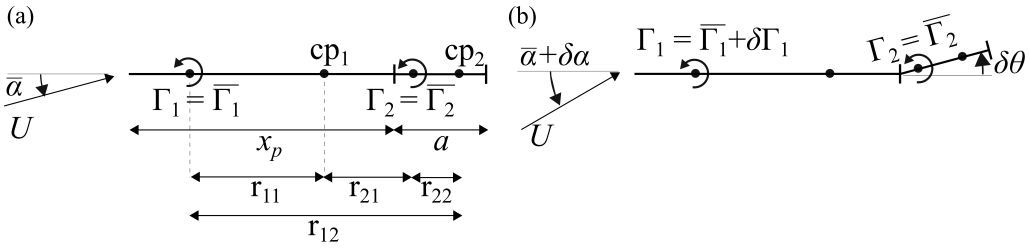

Figure 3: Two-panel model for flat plate with hinge with circulations Γ_1 and Γ_2 and collocation points cp_1 and cp_2 at (a) the mean flow condition and (b) after a change $\delta\alpha$ in the angle of attack.

In Fig. 3(a), the deflection of the flap is $\delta\theta = 0°$ and we can apply the boundary condition of no flow normal to the panel at the collocation points, such that

$$\mathrm{cp}_1 : \frac{\overline{\Gamma_1}}{2\pi \mathrm{r}_{11}} - \frac{\overline{\Gamma_2}}{2\pi \mathrm{r}_{21}} = -U\sin\overline{\alpha} \approx -U\overline{\alpha} \tag{8}$$

and

$$\mathrm{cp}_2 : \frac{\overline{\Gamma_1}}{2\pi \mathrm{r}_{12}} + \frac{\overline{\Gamma_2}}{2\pi \mathrm{r}_{22}} = -U\sin\overline{\alpha} \approx -U\overline{\alpha}. \tag{9}$$

We have said that the hydrodynamic moment about the flap hinge is fixed, so Γ_2 must be fixed. This means that when there is a change in the angle of attack $\delta\alpha$ (Fig. 3(b)), the flap moves but the lift on the flap portion does not change and so the new boundary conditions at cp_1 and cp_2 must be satisfied by changes in Γ_1. We define the boundary conditions in Fig. 3(b) as

$$\mathrm{cp}_1 : \frac{\overline{\Gamma_1} + \delta\Gamma_1}{2\pi \mathrm{r}_{11}} - \frac{\overline{\Gamma_2}}{2\pi \mathrm{r}_{21}} = -U(\overline{\alpha} + \delta\alpha) \tag{10}$$

and

$$\mathrm{cp}_2 : \frac{\overline{\Gamma_1} + \delta\Gamma_1}{2\pi \mathrm{r}_{12}} + \frac{\overline{\Gamma_2}}{2\pi \mathrm{r}_{22}} = -U(\overline{\alpha} + \delta\alpha) + U\delta\theta. \tag{11}$$

By substituting Eqs. 8 and 9 into Eqs. 10 and 11, we get

$$\delta\Gamma_1 = -2\pi \mathrm{r}_{11} U\delta\alpha \tag{12}$$

and

$$\delta\Gamma_1 = -2\pi \mathrm{r}_{12} U(\delta\alpha - \delta\theta). \tag{13}$$

Finally solving for $\delta\theta$ from Eqs. 12 and 13 and considering that $r_{11} = x_p/2$ and $r_{12} = 3c/4$, we find that

$$\delta\theta = \delta\alpha\left(1 - \frac{2x_p}{3c}\right). \tag{14}$$

For the foil tested in here, $x_p/c = 0.75$, and so the model gives $\delta\theta = \delta\alpha/2$. Recalling that Γ_2 is constant, the change in lift (δL_1) due to the change in angle of attack is computed from eq. 12, as

$$\delta L_1 = -\rho U\delta\Gamma_1 = 2\pi U^2 \rho \frac{x_p}{2}\delta\alpha \tag{15}$$

and the change in lift coefficient is

$$\delta C_L = \frac{\delta L_1}{\frac{1}{2}\rho U^2 c} = 2\pi\delta\alpha\frac{x_p}{c}. \tag{16}$$

We can normalise Eq. 16 by the load change encountered by a fully rigid foil, which is $2\pi\delta\alpha$. This gives us δC_L^*, the load relative to the rigid case:

$$\delta C_L^* = x_p/c. \tag{17}$$

Equivalently, the load reduction is

$$1 - \delta C_L^* = 1 - x_p/c = a/c. \tag{18}$$

The relationship between flap length to chord ratio and the load alleviation is therefore linear. For a flap extending over the rear 25% of the chord, the model predicts a 25% reduction in unsteady loading. This result is based on a quasi-steady approach, i.e. neglecting the fluid inertial effects and thus the time history of how the flow condition has reached the current state. In §4.2 this quasi-steady relationship will be compared with experimental results. However, to assess the reduced frequencies at which the quasi-steady model could fail because unsteady effects might become significant, we will first develop an unsteady model based on Theodorsen's theory.

2.2. Unsteady load alleviation effects

In order to assess the level of unsteady effects, and the deviation from the quasi-steady model above, we look at the predicted ratio of flap deflection amplitude (θ_0) to heave amplitude (h_0) for a heaving flat plate with a hinge in uniform flow. The total hydrodynamic moment acting on the hinge is given by Theodorsen [12], and it can be split into the hinge moment coefficient due to a heaving motion C_h and the hinge moment coefficient due to the flap motion C_h^f [13]. We have said that the moment around the flap does not change, therefore we can postulate that the hinge moment from heaving is exactly cancelled by the moment due to the flap motion, such that $C_h + C_h^f = 0$. Assuming harmonic motion for both heave and flap motion ($h = h_0 e^{i\omega t}$ and $\delta\theta = \theta_0 e^{i\omega t}$) and the corresponding time-derivatives ($\dot{h}, \ddot{h}, \delta\dot{\theta}, \delta\ddot{\theta}$), we can group the terms of equations C_h and C_h^f (the exact expressions for C_h and C_h^f can be found in Leishman [13]). By collecting terms, we derive an expression (see Appendix A) for the ratio of flap amplitude to heave amplitude in the form

$$\frac{\theta_0}{h_0} = \frac{-F\omega^2 + i\omega G}{-[B + D - \omega^2 A + i\omega(C + E)]}, \tag{19}$$

where A, B, C, D, E, F and G are defined in Appendix A and are all functions of the geometry (functions of parameters $T_1, T_2 ... T_{12}$ found in Theodorsen's paper [12]).

We multiply θ_0 by a to get the displacement amplitude of the flap ($a\theta_0$). Fig. 4 shows the ratio of $a\theta_0$ to h_0 predicted by the quasi-steady and unsteady models. The ratios are plotted as a function of the reduced frequency $k = \omega c/(2U)$. The quasi-steady model predicts a linearly increasing $a\theta_0/h_0$ ratio with increasing k (since the amplitude of the angle of attack fluctuation increases linearly with k for a foil in pure heave, see § 3.4), whereas the unsteady model predicts a more rapid increase with k. However, for $k < 0.35$ the two models predict virtually identical results.

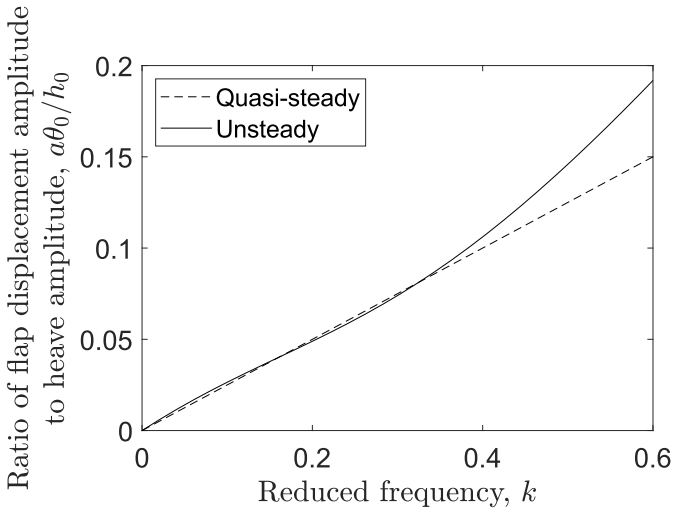

Figure 4: Ratio of flap displacement amplitude $a\theta_0$ to heave amplitude h_0 against reduced frequency predicted by quasi steady and unsteady models for $x_p = (3/4)c$.

A study assessing the effects of stiffness and damping on the flap deflection was also carried out (see Appendix A), and it was shown that due to the small stiffness and large damping coefficient (see Appendix B) the effects of these on the predicted flap deflection were small. As such, the quasi-steady model is likely to be sufficient for the frequency ranges tested in the experimental study below.

3. Experimental methodology

3.1. The foils

An extruded NACA 0012 profile was used to construct a rigid foil and a foil with a passive trailing-edge flap. The chord of both models was $c = 0.1\,\text{m}$ and the span was $S = 0.4\,\text{m}$. The CAD files are available in the Edinburgh Datashare repository (datashare.is.ed.ac.uk). The models were 3D printed in PLA material. Due to restrictions in the 3D print volume, the models were printed in two spanwise sections, with pins on the mating surfaces. The components were glued together with epoxy. The models had two attachment legs protruding from the upper surface at mid-span and mid-chord. The legs served as attachment point to a heaving mechanism and as a means of setting the angle of attack via a locking pin. The models were surface finished with a coating of matt black paint. In order to ensure 2D-in-the-mean flow conditions, the flow measurement plane (see Section A-A' in Fig. 5) was positioned away from the tank endwall, the join in the spanwise sections and the attachment point.

The foil with the passive trailing-edge flap was identical to the rigid foil, except that a hinge was placed at 75% of the chord so that the final part of the foil acted as a flap which was free to move about its leading edge. The flap was also 3D printed in two sections, which were hollow inside to provide maximum buoyancy. Six ball bearings connected the flap to the fore part of the

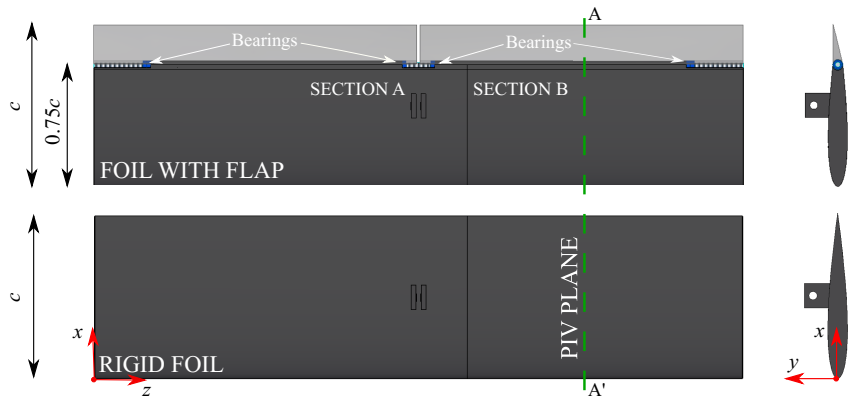

Figure 5: Top and side views of rigid foil and foil with passive trailing-edge flap, where the x, y and z-axes are oriented along the chordwise, normal and spanwise directions.

foil. The external diameter of the bearings was selected to match the thickness of the foil at the location of the pitching axis. The bearings were mounted on metal shafts that were threaded and secured to the body of the foil.

3.2. Heaving mechanism and water tunnel

Fig. 6 shows the experimental rig. It consisted of two linear motors that transmitted a heaving motion to the foil. The motors were triggered simultaneously with LabView and by prescribing a sinusoidal heaving motion to the motor drivers. The downstream motor was used to adjust the angle of attack of the foil. The bottom ends of the motors were connected to a six-millimetre-thick acrylic triangular support, which was connected at its lower end to the cable side of a six-axis load cell. The free side of the load cell was connected to an adaptor piece that held the foil in place. The adaptor had two supporting arms to reduce spanwise vibrations. Load cell measurements were sampled at 1000 Hz and data were acquired for 100 cycles in each test. Experiments were carried at $Re = 50,000$ and results were phase averaged. In all of the experimental runs, the motion of the rig and foil were started five full cycles prior to the force measurements. Hence, force startup transients did not affect the phase averaged results.

The rig was mounted in a free surface water tunnel at the School of Engineering, at the University of Edinburgh. The water tunnel is 9 m long, 0.4 m wide and 0.9 m high with a flat, horizontal bed. The mean water depth was set to 0.5 m and each foil was placed horizontally 0.25 m below the water surface. The foil heaved in uniform flow away from both the free surface and the bottom. The spanwise gap between the foil and the lateral wall of the tunnel was 5 mm on each side. Spanwise flow was minimised by keeping the gap between foil and flume side walls to a minimum, allowing the foil to move without friction but promoting two-dimensional flow. Inertial effects were measured in air and were subtracted from the values measured in water. The load cell was zeroed in still water prior to any measurement. Lastly, a steady state calibration was performed and the results are presented in Fig. 7, where it is shown that the steady state effect of the free surface and the rig was minimal at the angle of attack that we used.

We also note that the standing waves created by the changing cross-section of the triangular support were not significant, as shown in the supplementary material video ($k = 0.1, 2h_0/c = 0.3$).

Additionally, any free surface effects were minimised by orienting the suction side of the foil towards the flat, horizontal bed of the flume and by positioning the foil at the mid-height of the water column. PIV confirmed that the flow field was not altered by surface waves within the field of view of the camera.

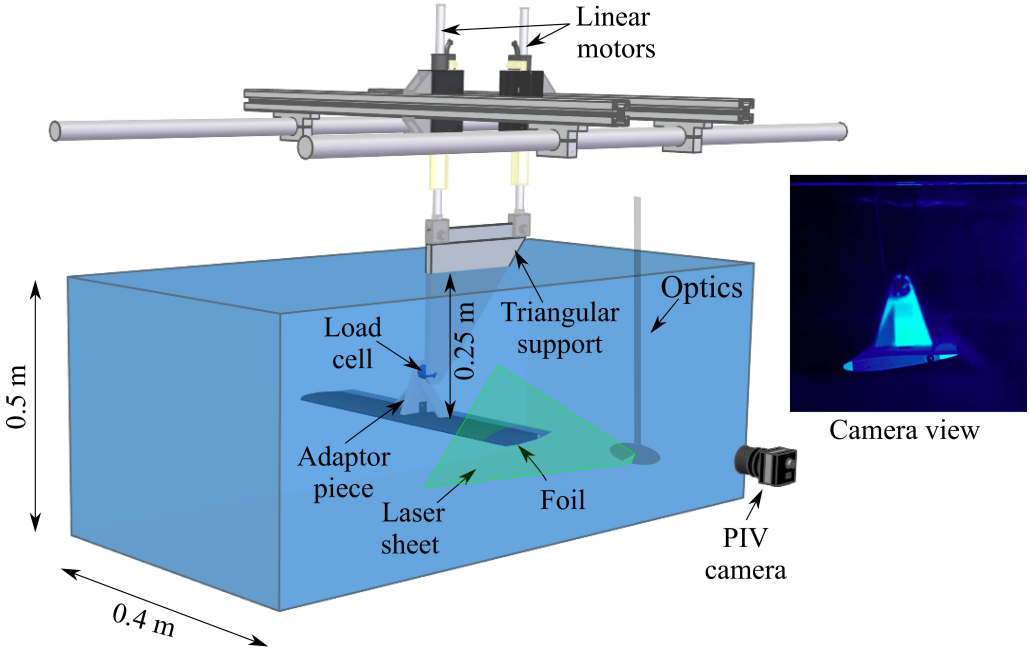

Figure 6: Heaving rig and foil with passive trailing-edge flap in the water tunnel with PIV camera and laser sheet. The camera view shows the foil with passive trailing-edge flap.

The Particle Image Velocimetry (PIV) system consisted of a Solo 200XT pulsed dual-head Nd:YAG laser, with an energy output of 200 mJ at a wavelength of $\lambda = 532$ nm. The camera was a CCD Imperx 5MP with a 2056 px $\times$ 2060 px resolution and a Nikkor f/2, 50 mm lens. Seeding particles comprised silver coated hollow glass spheres, with an average diameter of 14 µm and a density of 1.7 g/cc. The upper PIV sampling threshold was 7.5 Hz, therefore PIV image pairs were sampled at 2.4 Hz at $k = 0.1$ and at 7.2 Hz at $k = 0.3$ and $k = 0.5$ during 50 heaving cycles and the results were phase averaged. Two-pass adaptive correlation was applied. The first pass had a 64 px $\times$ 64 px interrogation window, with a Gaussian weighting and 50% window overlap. The second pass had a 24 px $\times$ 24 px interrogation window and a 75% window overlap. Finally, a 3 $\times$ 3 Gaussian filter was used to smooth the vector fields. To ensure a homogeneous distribution of particles, the flume was run 30 minutes prior to any PIV measurement. Stokes number (S_k) analysis was performed with $S_k < 0.1$, used as the threshold for acceptable flow tracking accuracy [14]. Although the PIV data in this paper was used qualitatively only, high correlation peak values, between 0.4 and 0.8, were ensured due to a high particle image density. The PIV uncertainty was estimated to be $u/U < 0.05$ and $v/U < 0.05$ via a quiescent measurement of the flow.

3.3. Steady-state measurements

The chord-normal (F_y) and chordwise (F_x) forces were measured for both foils for a set of experiments and post-processed with a Chebyshev type II low pass filter. The lift and drag forces were computed with

$$L = F_y \cos\alpha - F_x \sin\alpha \tag{20}$$

and

$$D = F_y \sin\alpha + F_x \cos\alpha, \tag{21}$$

where α is the angle of attack of the foil. The lift and drag coefficients (C_L, C_D) were computed by non-dimensionalising the force components by $0.5\rho U^2 A$.

The force measurements were validated by measuring the steady lift and drag force coefficients of the rigid foil at $Re = 50,000$ and for a range of angles of attack (α) between $-5°$ and $5°$. Results are shown in Fig. 7 and the measured lift coefficient is compared to data from Sheldahl and Klimas [15], and to $2\pi\alpha$. At negative angles of attack, the foil performance may be affected by the adaptor piece interfering with the flow on the suction side of the foil. However, for the remainder of the paper, the mean angle of attack is set to $5°$, where C_L and C_D show a good agreement with the literature.

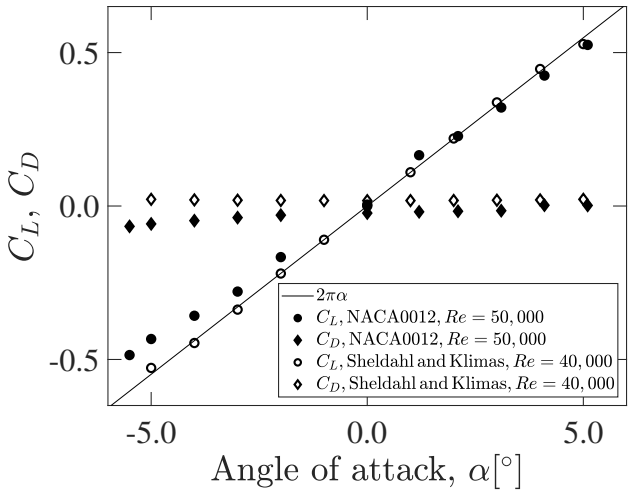

Figure 7: Measured time-averaged lift coefficient and time-averaged drag coefficient of rigid foil for a range of angles of attack between $-5°$ to $5°$ at $Re = 50,000$. Measured data compared to data by Sheldahl and Klimas [15] at $Re = 40,000$ and to $2\pi\alpha$.

3.4. Motion parameters

The kinematics of the foils are given by

$$h = h_0 e^{i\omega t} \qquad \dot{h} = i\omega h_0 e^{i\omega t} \qquad \ddot{h} = -\omega^2 h_0 e^{i\omega t}. \tag{22}$$

It is noted that the angle of attack variations encountered by tidal turbines are typically in the reduced frequency range $0 < k < 0.6$ [1, 3] and that changes in current speed due to large

but not rare regular waves result in angle of attack oscillations with amplitudes of about 5° [3].
185 In this work, three peak-to-peak heaving amplitudes ($2h_0/c = 0.1, 0.3, 0.5$) and three reduced frequencies ($k = 0.1, 0.3, 0.5$) were selected as representative of the tidal environment. These testing conditions correspond to angle of attack oscillations around the mean angle in the range of 0.6° to 14.0° (see Fig. 8). The larger angle of attack variations are intended to test limits of the validity of the proposed theoretical model.

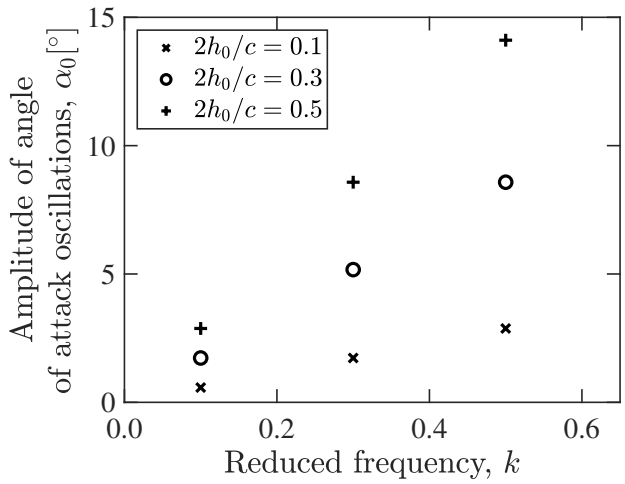

Figure 8: Amplitude of angle of attack oscillations (α_0) versus reduced frequency (k) for the nine tested cases.

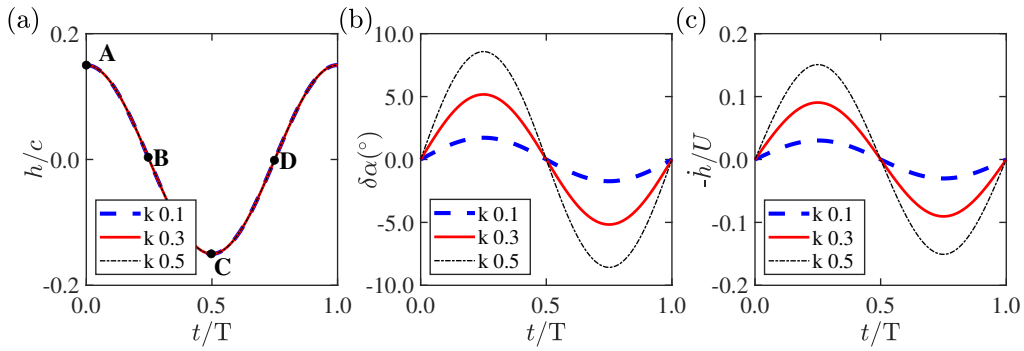

Figure 9: (a) Nondimensional heave displacement (h/c), (b) angle of attack variation ($\delta\alpha$) and (c) nondimensional heave velocity ($-\dot{h}/U$) for $2h_0/c = 0.3$ at $k = 0.1, 0.3$ and $k = 0.5$ during a normalised time period t/T.

Fig. 9 shows the nondimensional heave displacement (h/c), the angle of attack variation ($\delta\alpha$) in degrees and the nondimensional heave velocity ($-\dot{h}/U$) at the three tested reduced frequencies at a peak-to-peak amplitude of $2h_0/c = 0.3$. The zero position of different amplitude motions was located within 2% of mid-depth in the water tunnel. The angle of attack variations are defined by

$$\delta\alpha = \text{atan}\left(\frac{\dot{h}}{U}\right). \tag{23}$$

It can be inferred from Fig. 9(b) that the lift response leads the heave kinematics by approximately $\pi/2$.

3.5. Measurement of the flap rotation

The motion of the flap was measured for four cases: $2h_0/c = 0.3$ at $k = 0.1, 0.3, 0.5$ and $2h_0/c = 0.5$ at $k = 0.5$. For the lowest speed case ($2h_0/c = 0.3$, $k = 0.1$), it was possible to use photographs taken with an external light source, giving high spatial resolution (0.1% chord) and a total error of 0.1°. However, at the higher speed cases ($2h_0/c = 0.3$, $k = 0.3$, $2h_0/c = 0.3$, $k = 0.5$ and $2h_0/c = 0.5$, $k = 0.5$), the images were blurred due to the relatively long exposure time of the camera. In these latter cases, post-processed PIV images were used instead, as the short laser pulse duration (DT = 20 μs) eliminated any blur [16].

The flap was painted black and was not light reflective. This meant that it could be masked out with a threshold of brightness during PIV pre-processing and its motion measured by identifying the edge of the PIV data (in this case, streamwise velocity contours were chosen). The lower resolution (1% chord) of the PIV data means that this method has a larger error than the error from the photographs. The combined error in these measurements is estimated to be 0.5°.

In each cycle, angle measurements were taken at fifteen points at $2h_0/c = 0.3$, $k = 0.1, 0.3$ and at nine points at the $k = 0.5$ cases. A fit to the data with Fourier coefficients was calculated and described in §4.3 in order to find the amplitude of the flap motion. The flap deflection measurements described above are provided as supplementary material.

4. Results

Having introduced the theoretical and experimental methodologies, this section will compare the theory from §2 with the forces measured in the experiments. Theodorsen's unsteady lift theory [12] is used to predict the lift response of the rigid foil, and the quasi-steady formulation introduced in §2.1 (Eq. 17) is used to predict the load alleviation of the foil with the passive trailing-edge flap. The measured flap deflections are compared with predictions from both the quasi-steady and unsteady formulations. Lastly, near and far wake observations are related to the force and flap deflection findings.

4.1. Force measurements

As an initial example, we present in Figs. 10(a) and 10(b) the phase averaged lift and drag coefficients of both foils at one reduced frequency ($k = 0.3$) and at three different heave amplitudes ($2h_0/c = 0.1, 0.3$ and 0.5). The solid lines represent the data from the rigid foil and the dotted lines the data from the foil with the passive flap.

The passive trailing-edge flap reduces the peak-to-peak amplitude of the lift coefficient ($2\Delta C_L$) for all of the cases in Fig. 10(a). The flap does not appear to have a negative impact on the drag

coefficient (C_D), as indicated in Fig. 10(b). Similar trends are observed for the lift and drag coefficients for the remaining tested reduced frequencies ($k = 0.1, 0.5$). Measurement errors in ΔC_L and ΔC_D are estimated to be ±5%.

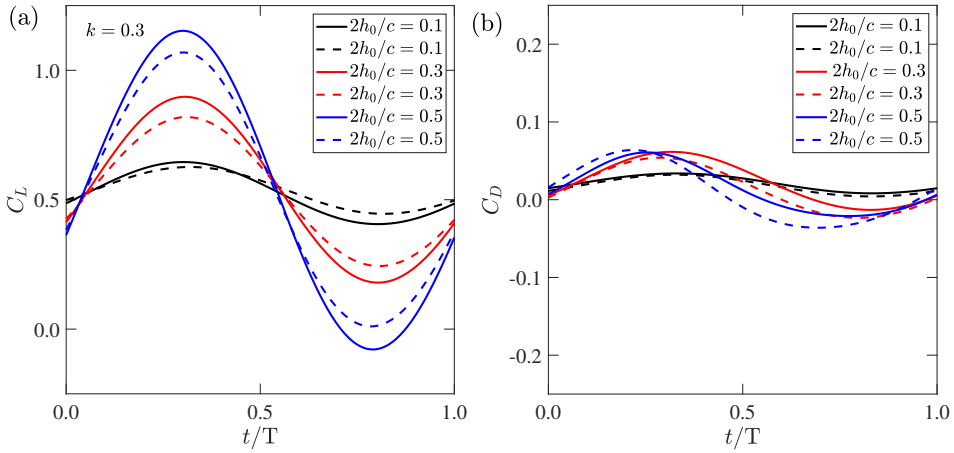

Figure 10: Phase averaged (a) lift and (b) drag coefficient of rigid foil (solid lines) and foil with flap (dashed lines), at $k = 0.3$ and $2h_0/c = 0.1, 0.3$ and 0.5 during a normalised time period t/T.

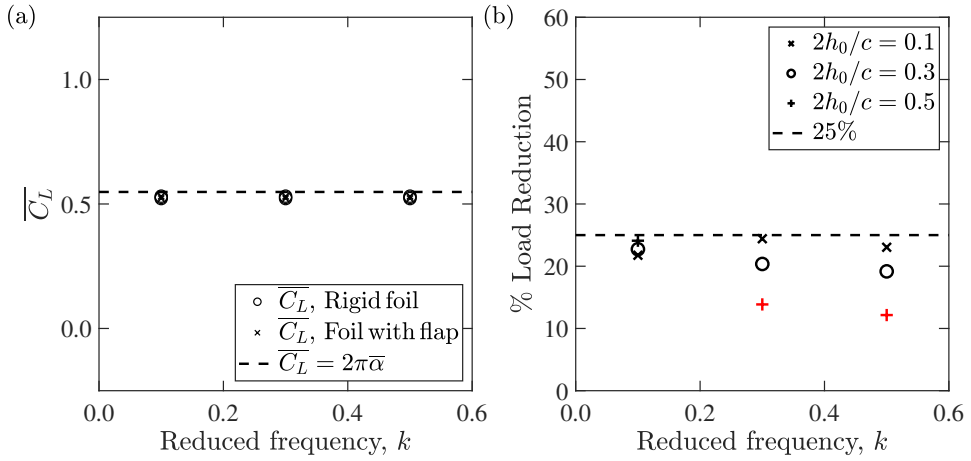

Figure 11: (a) Mean lift coefficients ($\overline{C_L}$) for rigid foil and foil with flap and (b) ΔC_L ratio between foil with flap and rigid foil, at three reduced frequencies ($k = 0.1, 0.3, 0.5$) and three displacement amplitudes ($2h_0/c = 0.1, 0.3, 0.5$).

The mean lift coefficients ($\overline{C_L}$) for the rigid foil and the foil with the flap are presented in Fig. 11(a) for all of the 9 tested cases. The mean values corresponding to $k = 0.1, 0.3, 0.5$

are identified along the horizontal axis, and the results for the three values of $2h_0/c$ (0.1, 0.3, 0.5) collapse on top of each other at every k. The dotted line denotes the ideal C_L of $2\pi\overline{\alpha}$, where $\overline{\alpha} = 5°$. The mean lift coefficients ($\overline{C_L}$) are independent of the reduced frequency and the displacement amplitudes. Hence, if the foil with the flap represents a turbine blade section, it would not compromise the mean power output for any flow condition.

The ratio between ΔC_L of the foil with the flap and the rigid foil is shown as a percentage in Fig. 11(b). It is found that the load alleviation lies between 20% and 25% for most of the tested cases. The load alleviation tends to drop in cases where both the reduced frequency and the motion of the amplitude are large ($k \geq 0.3$, $\alpha_0 > 9°$). In the two most extreme cases ($2h_0/c = 0.5$, $k = 0.3$ and 0.5, plotted in red), the load alleviation drops to about 15%. This will be discussed in greater detail in §4.4.

4.2. Force modelling

For all of the tested cases, the measured lift coefficient amplitude (ΔC_L) is compared to that computed with Theodorsen's lift equation for heaving motion. The equation can be found in, for example, McGowan et al. [17].

Following the procedure laid out by Young and Smyth [18], the measured lift coefficient amplitude is computed with

$$\Delta C_L = \sqrt{A_\mathrm{N}^2 + B_\mathrm{N}^2} \tag{24}$$

and the phase with

$$\phi = \tan^{-1}\left(\frac{A_\mathrm{N}}{B_\mathrm{N}}\right), \tag{25}$$

where A_N and B_N are the Fourier coefficients

$$A_\mathrm{N} = \frac{2}{M}\int_0^M L(t)\sin(2\pi f_h t)dt \tag{26}$$

and

$$B_\mathrm{N} = \frac{2}{M}\int_0^M L(t)\cos(2\pi f_h t)dt, \tag{27}$$

where $L(t)$ is the lift force signal, M is the length of the signal and f_h is the heave frequency.

Results for the lift coefficient amplitudes (ΔC_L) are presented in Fig. 12(a) and plotted as a function of the reduced frequency (k) for three different values of $2h_0/c$. For all of the cases, the measured ΔC_L of the foil with the flap (circular markers) is lower than the measured ΔC_L of the rigid foil. In Fig. 12(a), ΔC_L of the foil with the flap (dashed-dotted line) is modelled by the ΔC_L computed with Theodorsen's lift equation multiplied by $1 - a/c = 0.75$. This factor was derived in §2.1.

For the more extreme cases (high reduced frequency and high incidence change), the data deviates from Theodorsen's function and the quasi-steady load alleviation model overestimates the load mitigation provided by the foil with the flap. This could be associated with the angle of attack oscillations being large and causing flow separation. The flow field will be investigated with PIV in §4.4.

The phase response (ϕ) of the rigid foil and foil with the flap is plotted in Fig. 12(b). In contrast to the lift coefficient amplitudes, there is no significant difference between the phase response of the rigid foil and the foil with the flap. Theodorsen's model (solid line) predicts the trend of the phase response qualitatively. A latency of 100 ms is included to account for delays in the linear actuator control.

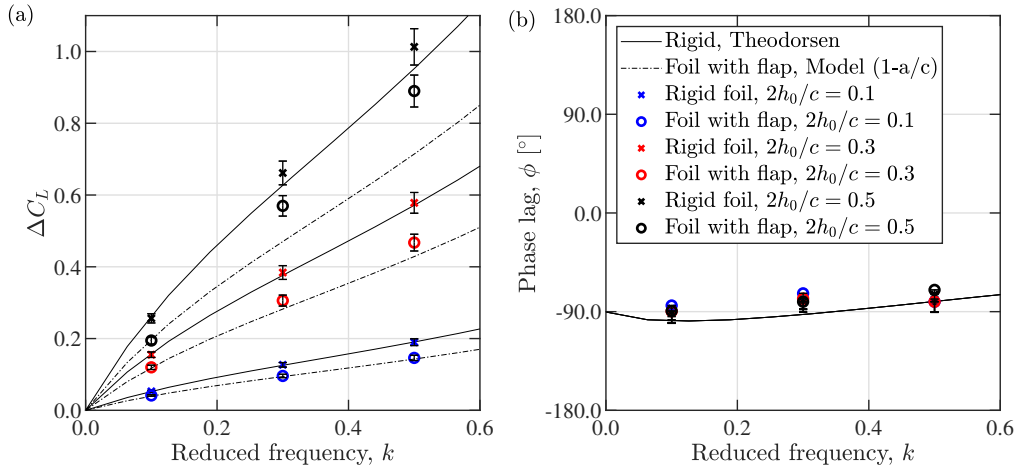

Figure 12: (a) Amplitude of lift coefficient (ΔC_L) for rigid foil and foil with flap, and (b) phase lag (ϕ) of rigid foil and foil with flap at three reduced frequencies (k = 0.1, 0.3 and 0.5) and at three non-dimensional heaving displacements ($2h_0/c$ = 0.1, 0.3, 0.5).

4.3. Flap motion

As introduced in §3.5, the flap motion was measured in four cases: $2h_0/c = 0.3$ at $k = 0.1, 0.3, 0.5$ and $2h_0/c = 0.5$ at $k = 0.5$. This set of tests covers two cases in which the load alleviation is close to the predicted value of 25%, one in which it is significantly lower than the prediction ($2h_0/c = 0.5$, $k = 0.5$) and one which is on the borderline ($2h_0/c = 0.3$, $k = 0.5$).

Figs. 13(a), (b), (c) and (d) show the measured flap deflection ($\delta\theta$) against non-dimensional time for the four cases. The measurements are shown with scattered circular markers. A sinusoidal fit was constructed using the first order Fourier coefficient for Figs. 13(a), (b) and (c) and the first and second order Fourier coefficients for Fig. 13(d). It is noted that two Fourier coefficients are needed to capture salient features of the data, such as shedding LEVs, and that some asymmetry in the measurement is expected due to LEVs shedding only in half of the heaving cycle. The deflection of the flap predicted by the quasi-steady and unsteady model are plotted as well. We recall that α_0 is the amplitude of the angle of attack oscillations, which is plotted in Fig. 8 for the different tested cases, and that $\delta\alpha$ is the inflow angle of attack oscillation.

Fig. 13(a) and Fig. 13(b) show that the amplitude and the phase of the flap deflection predicted by both models agree with the measured data when k and $2h_0/c$ are low. This occurs when α_0 is less than or equal to 5°. In these cases, $\delta\theta$ is approximately $\delta\alpha/2$, as predicted in Eq. 14. These two cases also showed a load reduction of approximately 25%, in line with the quasi-steady model (see Fig. 11(b)).

In contrast, in the cases shown in Fig. 13(c) and Fig. 13(d) both models over estimate $\delta\theta$. This occurs when α_0 approaches or surpasses 9°. In these two latter scenarios, $\delta\theta < \delta\alpha/2$, and the load alleviation is less than 25% (see Fig. 11(b)). It is hypothesised that flow separation reduces the loading on the flap and therefore the flap deflects less compared to the prediction of both models (see next section, §4.4). The phase is also affected. In fact, the measured deflection lags approximately $\pi/2$ to that of the predicted unsteady response.

When $2h_0/c = 0.5$ and $k = 0.5$, the most extreme case, a double peak is detected in the scattered points of Fig. 13(d). This double peak is not captured by either of the models and is related to a leading edge vortex (LEV), as discussed in §4.4.

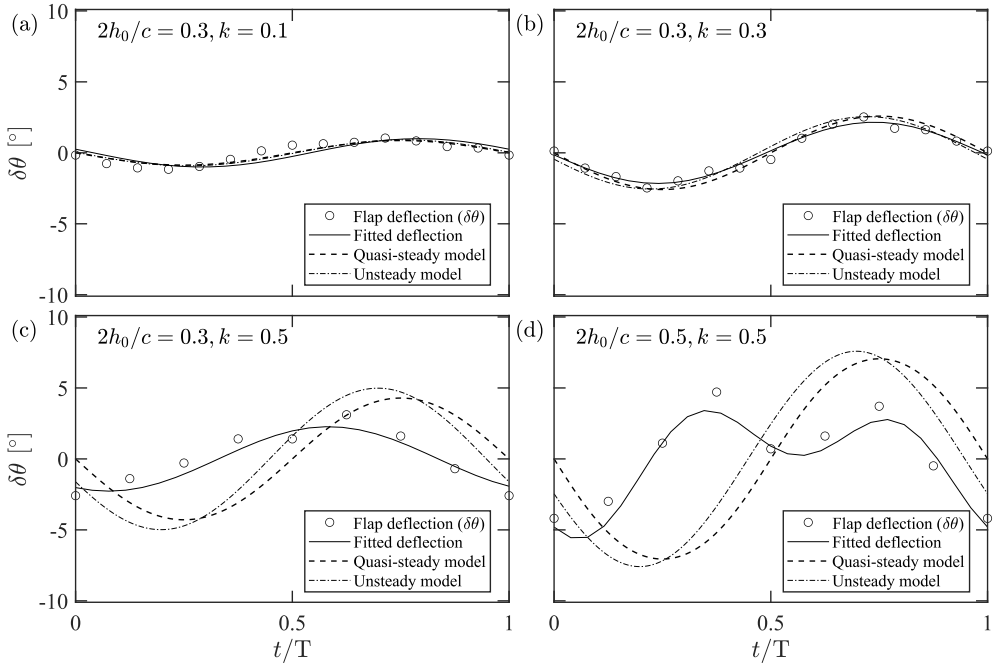

Figure 13: Measured, fitted and computed (quasi-steady and unsteady) flap deflection at $2h_0/c = 0.3$ and $k = 0.1, 0.3, 0.5$ and at $2h_0/c = 0.5$ and $k = 0.5$.

4.4. Vorticity Field

From Fig. 9(a) it can be seen that the lowest point of the downstroke is at time C in the cycle, which corresponds to a non-dimensional time of $t/\mathrm{T} = 0.5$. This point is where the largest flow separation occurs in all cases, in line with the findings of Bird et al. [19, 20]. In this section we therefore focus on the flowfield at time C and time C*, which is one measured time-step before C ($t/\mathrm{T} = 0.38$ in the case of $k = 0.5$).

To investigate the flow field of cases where the performance of the load mitigation model deteriorates, contours of nondimensional vorticity (blue-to-red colour scale) and γ_2 (black lines) are shown in Figs. 14 and 15 at $2h_0/c = 0.3$ and at $2h_0/c = 0.5$, both at $k = 0.5$, which are two of the most extreme cases. The γ_2 criterion is a global detection scheme [21, 22] to identify vortices in the flow. The detection threshold is set to $\gamma_2 = 2/\pi$ and more details of the algorithm can be found in, for example, Arredondo-Galeana and Viola [23]. In Figs. 14 and 15, the $\gamma_2 = 2/\pi$ isocontour is used to identify an LEV.

For $2h_0/c = 0.3$ and $k = 0.5$, the vorticity contours in Fig. 14 show a thick layer of vorticity convecting along the foil. In position C, the γ_2 contours highlight segmented vorticity on the surface of the foil with the flap (Fig. 14(d)), as opposed to a more coherent LEV in the rigid

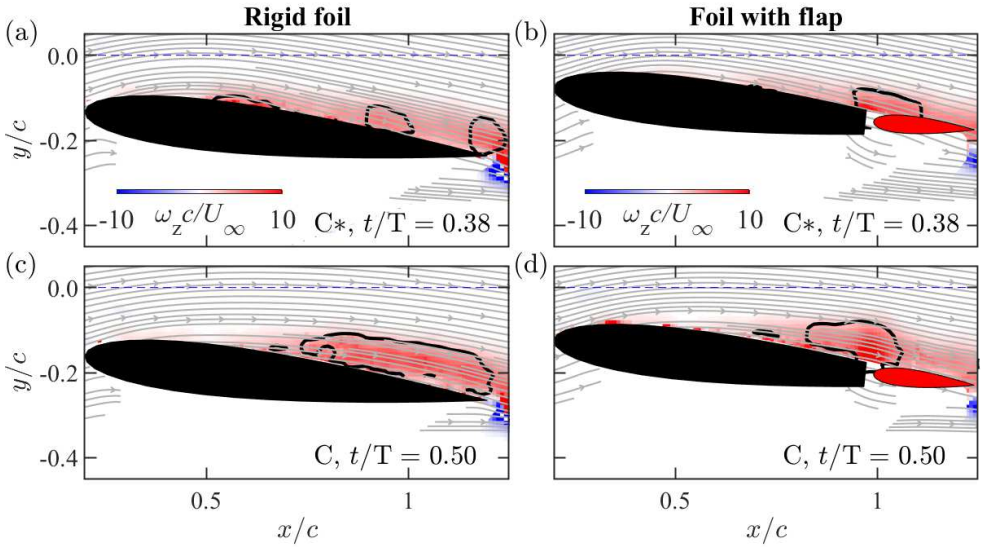

Figure 14: Near wake of rigid foil and foil with flap at $2h_0/c = 0.3$ and $k = 0.5$, at C* and C.

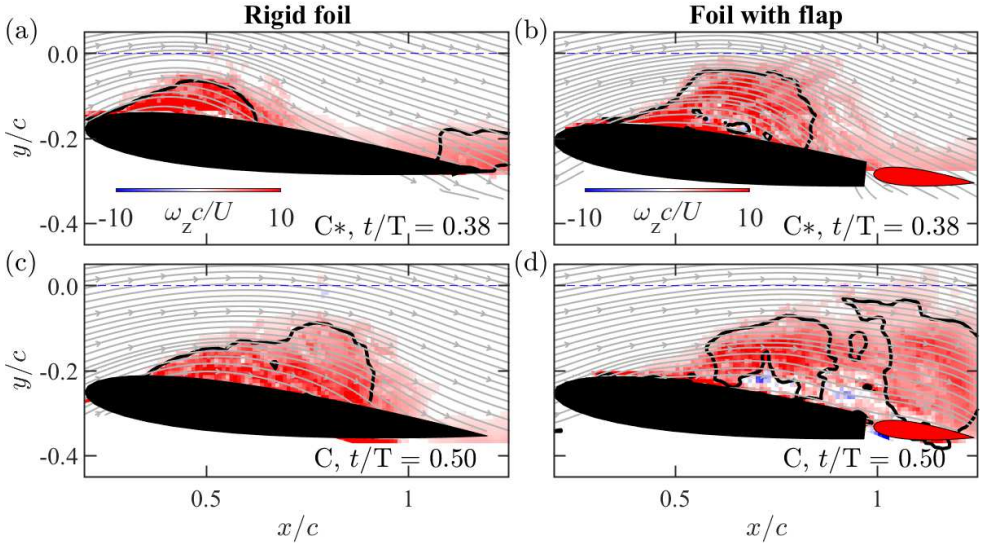

Figure 15: Near wake of rigid foil and foil with flap at $2h_0/c = 0.5$ and $k = 0.5$, at C* and C.

model (Fig. 14(c)). This segmentation of vorticity is due to the flap discontinuity in the foil. At time C, significant flow separation occurs and it reduces the loading on the flap and causes the flap to deflect less than in attached flow conditions (see Appendix C for data from cases where the flow remains attached). This reduced deflection was shown in Fig. 13(c) and the analytical

Table 1: Summary of load alleviation, flap motion and LEV observations.

k	$2h_0/c$	% Load alleviation	Flap motion $\delta\theta/\delta\alpha$	LEV?	Double peak?
0.1	0.1	22	-	-	-
	0.3	23	0.47 ±12%	No	No
	0.5	24	-	-	-
0.3	0.1	24	-	-	-
	0.3	20	0.42 ±23%	No	No
	0.5	14	-	-	-
0.5	0.1	23	-	-	-
	0.3	19	0.25 ±23%	Yes	No
	0.5	12	0.26 ±14%	Yes	Yes

formulation starts overestimating load alleviation, as shown in Fig. 12(a).

Fig. 15 shows the condition at $2h_0/c = 0.5$ and $k = 0.5$. The γ_2-contours in Figs. 15(c) and 15(d) highlight a stronger LEV than in the case shown in Fig. 14. As with the previous case, flow separation reduces the loading and the motion of the flap, compared to those of attached flow conditions. The strong LEV induces a chord-normal velocity at the flap, changing the flap circulation Γ_2 and thus $\delta\theta$ (cf. Eqs. 8-11). The sign of the induced velocity changes as the centroid of LEV advects downstream along the flap, resulting in an opposite effect on $\delta\theta$ and thus explaining the double peak previously detected in Fig. 13(d).

Appendix C shows nondimensional vorticity and γ_2 from all four non-dimensional times ($t/\mathrm{T} = 0.0, 0.25, 0.50$ and 0.75) for all of the cases presented in Fig. 13, ($2h_0/c = 0.3$ and $k = 0.1, 0.3$ and 0.5 and for $2h_0/c = 0.5$ and $k = 0.5$) and Table 1 summarises the results in terms of flap motion and PIV measurements. It can be concluded that under attached flow conditions, the flap motion amplitude is half of that of the angle of attack variation, and no LEV is observed. When the flow separates, the flap rotation is reduced and an LEV is convected downstream along the chord of the foil. When the LEV has a sufficient strength, it causes a double peak in the flap motion. In other words, the quasi-steady model derived in §2 predicts the behaviour of the flap and the associated load alleviation accurately in cases when the flow remains attached.

5. Conclusions

In this paper we have considered a foil that heaves sinusoidally in a uniform stream and investigated whether a trailing-edge flap connected through a torsional spring could alleviate the load fluctuations without affecting the mean load. Through the development of a theoretical model, we have shown that a highly flexible spring with a high preload can achieve this, and that the spring moment is almost constant for small angle of attack fluctuations. Furthermore, the model reveals that the fraction of load alleviation is given by the relative size of the flap and the foil. Specifically, the fraction of load alleviation is a/c, where a is the length of the flap and c is the total chord of the foil including the flap. The flap rotates by a fraction of the angle of attack variation - a fraction that depends linearly on a/c.

These results were achieved with a quasi-steady model. We used Theodorsen's theory to predict the limit of validity of this model as the reduced frequency increases. We found that the unsteady effects are negligible at reduced frequencies $k < 0.35$.

We verified these theoretical findings for one flap length. We undertook water tunnel tests of a rigid foil and a foil with a passive trailing-edge flap extending over the last 25% of the chord ($a/c = 0.25$). For a foil with a passive trailing-edge flap with $a/c = 0.25$, the theoretical model predicts 25% load alleviation and a flap motion of 50% of the incidence variation. The experimental data matches these predictions within the experimental uncertainty as long as the amplitude of the angle of attack variation is lower than about 9°. At combinations of reduced frequencies and heave amplitudes resulting in higher angle of attack amplitudes, the load alleviation decreases. Analysis of the flow field with particle image velocimetry reveals that the theoretical model loses accuracy when significant flow separation occurs and a shed leading edge vortex interferes with the flap motion.

Overall these results demonstrate that a foil with a passive trailing-edge flap can mitigate unsteady loading without compromising the mean loads.

CRediT authorship contribution statement

Abel Arredondo-Galeana: Writing - original draft, Methodology, Formal analysis, Investigation, Experiments, Postprocessing.

Anna Young: Writing - review & editing, Conceptualization, Supervision, Funding acquisition.

Amanda Smyth: Writing - review & editing, Methodology, Formal analysis, Investigation.

Ignazio Maria Viola: Writing - review & editing, Conceptualization, Supervision, Funding acquisition

Declaration of Competing Interest

The authors declare that they have no known competing financial interests or personal relationships that could have appeared to influence the work reported in this paper.

Acknowledgements

This work received funds from Wave Energy Scotland (WES) and the UK Engineering and Physical Sciences Research Council (EPSRC) via the EPSRC Centre for Marine Energy Research (EP/P008682/1), the EPSRC Centre for Advanced Materials for Renewable Energy Generation (EP/P007805/1), as well as research grants EP/M02038X/1 and EP/R511687/1. The authors would like to thank Geethanjali Pavar, Gabriele Pisetta and Shuji Otomo for the insightful discussions that enriched this work.

Forces and PIV measurements are available in the Edinburgh Datashare repository (datashare.is.ed.ac.uk).

Appendix A.

This appendix shows, initially, the derivation of Eq. 19, which is the ratio of the flap deflection amplitude θ_0 to the heaving amplitude h_0 computed with Theodorsen's theory.

In §2.2, we have said that because the moment around flap does not change, we can postulate that the hinge moment from heaving is cancelled by the hinge moment due to the flap motion, such that

$$C_h + C_h^f = 0, \tag{A.1}$$

where C_h is the hinge moment coefficient due to motion of the foil and C_h^f is the hinge moment coefficient due to the motion of the flap. For a heaving motion, and following the definitions in Leishman [13], the moment coefficients are

$$C_h = \frac{T_1 b\ddot{h}}{2U^2} - \frac{T_{12}C(k)\dot{h}}{2U} \tag{A.2}$$

and

$$C_h^f = \frac{T_3 b^2\ddot{\theta}}{2U^2\pi} - \frac{T_{12}T_{10}C(k)\theta}{2\pi} - \frac{T_{12}T_{11}C(k)b\dot{\theta}}{4\pi U} - \frac{(T_5 - T_4T_{10})\theta}{2\pi} + \frac{bT_4T_{11}\dot{\theta}}{4U\pi}, \tag{A.3}$$

where $T_1, T_2...T_{12}$ are defined in Theodorsen's manuscript [12] and b is the semi-chord. In Eqs. A.2 and A.3, the heaving motion kinematics are

$$h = h_0 e^{i\omega t} \qquad \dot{h} = i\omega h_0 e^{i\omega t} \qquad \ddot{h} = -\omega^2 h_0 e^{i\omega t} \tag{A.4}$$

and the flap motion kinematics are

$$\theta = \theta_0 e^{i\omega t} \qquad \dot{\theta} = i\omega\theta_0 e^{i\omega t} \qquad \ddot{\theta} = -\omega^2\theta_0 e^{i\omega t}, \tag{A.5}$$

where h_0 and θ_0 are the amplitudes of the heaving motion and the flap deflection. By defining

$$A \equiv T_3 b^2/2\pi U^2, \quad B \equiv -T_{12}T_{10}C(k)/2\pi, \quad C \equiv -T_{12}T_{11}bC(k)/4\pi U,$$
$$D \equiv -(T_5 - T_4T_{10})/2\pi, \quad E \equiv T_4T_{11}b/4\pi U, \quad F \equiv T_1 b/2U^2 \text{ and } G \equiv -T_{12}C(k)/2U$$

and substituting the motion kinematics in Eqs. A.2 and A.3, we can rewrite Eq. A.1 as:

$$h_0[-F\omega^2 + i\omega G] + \theta_0[B + D - \omega^2 A + i\omega(C + E)] = 0. \tag{A.6}$$

Finally we can solve for the θ_0/h_0 ratio

$$\frac{\theta_0}{h_0} = \frac{-F\omega^2 + i\omega G}{-[B + D - \omega^2 A + i\omega(C + E)]}, \tag{A.7}$$

which is Eq. 19 in §2.2.

Secondly, we show the effect of coupling a spring mass damper system to the unsteady flap motion of the flap, such that

$$I\delta\ddot{\theta} + \gamma\delta\dot{\theta} + k_s\delta\theta = X(C_h + C_h^f), \tag{A.8}$$

where I is the moment of inertia of the flap, γ is the damping constant, k_s is the stiffness constant and $X = 0.5\rho U^2 c^2 l$, where l is the span of the blade. Similarly to the workings to get Eq. A.6, we obtain the following expression

$$\theta_0[-\omega^2 I + i\omega\gamma + k_s - X(B + D - \omega^2 A + i\omega(C + E))] = Xh_0[-F\omega^2 + i\omega G]. \tag{A.9}$$

Dividing terms by k_s and using the definitions of the damping ratio

$$\zeta = \frac{\gamma}{2\omega_n I} \tag{A.10}$$

and of the squared natural frequency

$$\omega_n^2 = \frac{k_s}{I}, \tag{A.11}$$

we get

$$\theta_0\left[-\frac{\omega^2}{\omega_n^2}+i\frac{2\zeta\omega}{\omega_n}+1-\frac{X}{k_s}\left(B+D-\omega^2A+i\omega(C+E)\right)\right]=\frac{Xh_0}{k_s}\left[-F\omega^2+i\omega G\right]. \tag{A.12}$$

Finally, the θ_0/h_0 ratio in the coupled model is

$$\frac{\theta_0}{h_0}=\frac{X}{k_s}\left[\frac{-F\omega^2+i\omega G}{1-\frac{\omega^2}{\omega_n{}^2}-\frac{X}{k_s}(B+D-\omega^2A)+i\omega\left[\frac{2\zeta}{\omega_n}-\frac{X}{k_s}(C+E)\right]}\right]. \tag{A.13}$$

375 In Fig. A.16, we plot $a\theta_0/h_0$ versus k, where a is the length of the flap and $a\theta_0$ represents the displacement amplitude of the flap. Results are presented for the quasi-steady, unsteady, coupled models and experimental measurements. The values for U, b, ζ, k_s, ω_n utilised in the unsteady and coupled models are all actual values from the experiment. The dynamic parameters (ζ, k_s, ω_n) are measured with a step test on the flap in Appendix B.

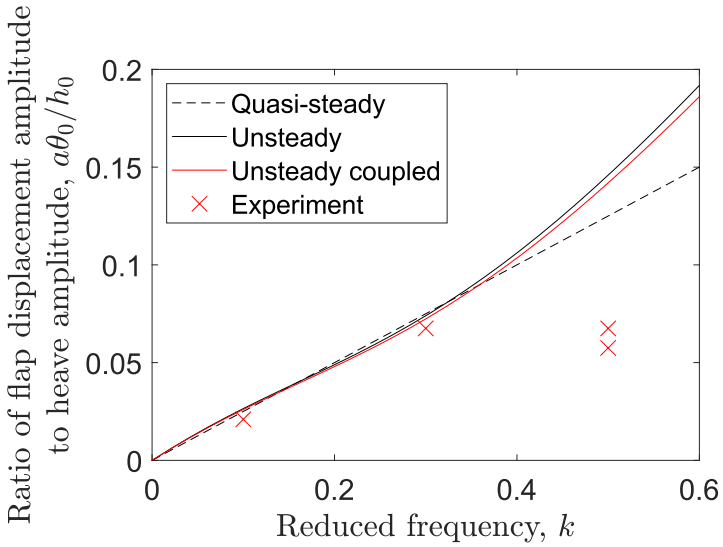

Figure A.16: Flap displacement amplitude ($a\theta_0$) to heave amplitude (h_0) ratio predicted by the quasi-steady, unsteady and coupled models versus experimental measurements

380 We find that both unsteady and unsteady coupled models predict a similar response in the range of $0 < k < 0.5$. The experimental results are reasonably predicted for $0 < k < 0.35$, where the flow remains attached. As the flow separates, in the range of $k \geq 0.35$, both models overestimate the loading on the flap and the prediction becomes inaccurate. It is to note that in this range, coupling damps the response slightly.

Appendix B.

In this Appendix we consider the mechanical frequency response of the flap in order to verify firstly that the flap can respond to the input frequencies used in the tests and secondly that it behaves as if attached to the main foil by a torsional spring with low stiffness and high pre-load angle, as required for the model presented in §2.

A step response test was performed on the flap in the tunnel with the water switched on and with the blade at its equilibrium position. The flap was deflected externally from equilibrium and then released to measure the natural frequency (f_n). The test also showed high-frequency flap oscillations due to rig vibrations. Fig. B.17(a) shows the step response of the vertical force component (F_y) of the foil with the flap. The black line shows the raw force signal, the red line the force filtered signal and the pink line an ideal step response. In the test, the settling time T_0 is estimated to be 2 seconds and this is used to normalise the the x-axis of Fig. B.17(a). Additionally, the blue line shows the step response of a second order system modelled with a damping ratio of $\zeta = 1.7$ and with a natural angular frequency $\omega_n = 2\pi f_n$.

It is observed that the range of periods for the heaving motion experiments (T = 1.25 s to 6.25 s) ranges from $0.63T_0$ to $3.10T_0$. This could be a concern at high frequencies, but we note that the step response was performed with a flap deflection that exceeded the maximum deflection encountered in the heaving motion tests, and that at $0.5T_0$, the flap has already reached about 90% of the final step response value. Hence, although the step is not a sinusoidal input, it shows that the flap responds effectively to the range of frequencies and angle of attack oscillation amplitudes that were tested in the experiments.

Fig. B.17(b) shows the power spectral density of the raw and filtered force step response, in black and red respectively. The first peak, in both of the power spectral density plots, corresponds to the natural frequency and is equal to $f_n = 1.4$ Hz. This peak corresponds to the large scale oscillations of the step response visible in Fig. B.17(a). The second peak, in the raw signal occurs at around $f = 18$ Hz and is due to vibrations of the rig in normal operation and corresponds to the small scale frequency of oscillations (Fig. B.17(a)). A low-pass filter was set to $f = 5$ Hz in the post-processing of force signals, to filter out the high frequency vibrations of the flap.

Fig. B.18 shows the power spectral density of the normal force (F_y) signal for all the tested heaving amplitudes ($2h_0/c$) and reduced frequencies (k). Results are presented in subgroups of the same $2h_0/c$ but different k. Fig. B.18(a) shows $2h_0/c = 0.1$, Fig. B.18(b) shows $2h_0/c = 0.3$ and Fig. B.18(c) shows $2h_0/c = 0.5$. Frequency peaks are visible at $f = 0.16, 0.48$ and 0.80, in the three subfigures and correspond to $k = 0.1, 0.3$ and 0.5, respectively. The solid and the the dashed lines represent the rigid foil and the foil with the flap, respectively and no discernible change in the peak frequencies between the foils is observed. It is important to note that the magnitudes of the forces from the natural frequency of the flap and that of the oscillations (Fig. B.17(b)) are much smaller than the loading due to heaving (Fig. B.18). Additionally the heave frequencies are located to the left hand side of the natural frequency of the flap. The harmonic peak shown in Fig. B.18(c) at $2h_0/c = 0.5$ and $k = 0.5$ could be the effect of the induced velocities of two LEVs in the near wake of the foil during one heave cycle (positions C and D of Fig. C.22 in Appendix C).

Let us consider the natural angular frequency of a torsional harmonic oscillator

$$\omega_n = \sqrt{\frac{k_s}{I}} = 2\pi f_n, \tag{B.1}$$

Considering the flap system as a torsional harmonic oscillator with a mass of a 100 g, its moment

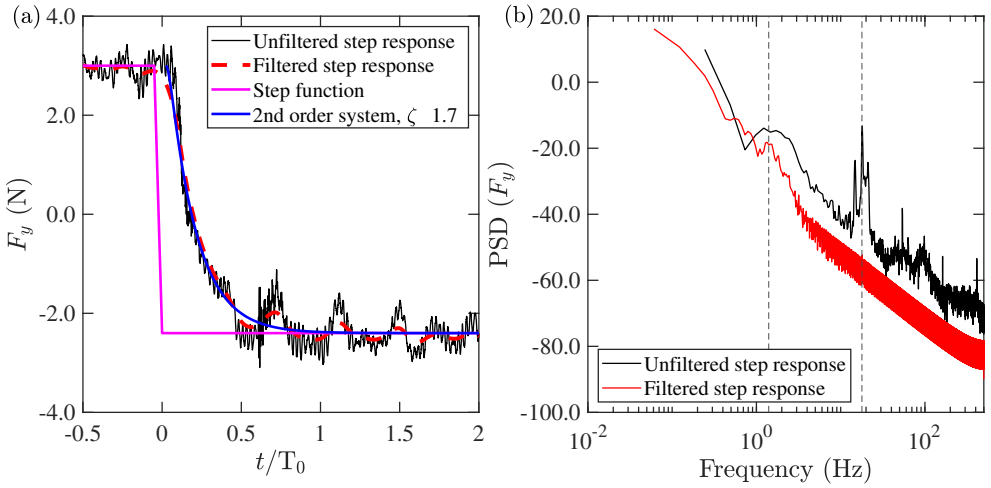

Figure B.17: a) Imposed disturbance on flap at equilibrium state showing unfiltered, filtered, ideal and modelled step response of the normal force (F_y) on the foil with the flap and b) frequency response to disturbance of filtered and unfiltered signals. First peak corresponds to natural frequency of the system (f_n), second peak corresponds to frequency of flap oscillations due to rig vibrations

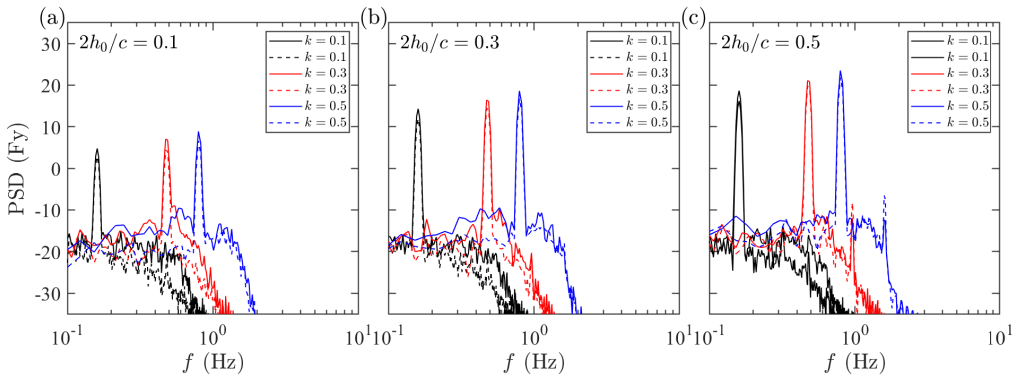

Figure B.18: Power spectral density of instantaneous normal force (F_y) of rigid foil and foil with the flap at $f = 0.16, 0.48$ and 0.80 ($k = 0.1, 0.3$ and 0.5) and $2h_0/c = 0.1, 0.3$ and 0.5

of inertia is estimated as $I = mr^2$. Here, r is assumed to be one third of the length of the flap, at the centre of mass, and equal to $r = c/12 = 0.0083$ m. The foil with the flap does not actually have a torsional spring, because the constant moment is applied by the buoyancy force. However, a hypothetical torsional spring coefficient can be computed by utilising Eq. B.1. Hence it is found that $k_s = 0.0005$ Nm/rad. The preload angle (θ_p) of the hypothetical torsional spring can be computed by equating the torsional spring moment to the buoyancy moment that acts on

the flap. The buoyancy force is equal to

$$B = \rho g V, \tag{B.2}$$

where g is the acceleration due to gravity and V is the volume of the flap. The volume being equal to the cross-sectional area of the flap (S_1) times the span (l). By considering that $\rho = 1000\,\mathrm{kg/m^3}$, $g = 9.81\,\mathrm{m/s}$, $l = 0.4\,\mathrm{m}$ and $S_1 = 7.5x10^{-5}\,\mathrm{m^2}$, the estimated buoyancy force is equal to $B = 0.3\,\mathrm{N}$. The constant moment due to buoyancy force is then

$$M_B = \frac{1}{12} cB, \tag{B.3}$$

where $c/12$ is the arm length of the buoyancy moment. Hence M_B acting on the flap is equal to
435 $0.0025\,\mathrm{Nm}$. The weight of the flap (W) is neglected in the moment balance because $B \gg W$, due to the density of water. If we equate the buoyancy moment to the torsional moment ($M_B = k_s\theta_\mathrm{p}$), then a torsional spring with a stiffness coefficient of $k_s = 0.0005\,\mathrm{Nm/rad}$ and a preload $\theta_\mathrm{p} = 5\,\mathrm{rad}$ (about $5/6^{\mathrm{th}}$ of full turn) can provide an equivalent moment to M_B. In essence, such system would be a low stiffness mechanism, such as the one described in §2.

Appendix C.

This Appendix shows the phase averaged flowfields at four positions of the heaving kinematics. The positions are labelled as A, B, C and D and correspond to the locations in the displacement curve defined in Fig. 9(a). Positions A to C describe one full downstroke, where C is the bottom of it. It can be seen in Figs. C.19 and C.20, that at heave displacement amplitudes of $2h_0/c = 0.3$ and at reduced frequencies of $k = 0.1$ and 0.3 the wake remains straight and no trailing-edge separation occurs. On the contrary, in Fig. C.21, at the same $2h_0/c$ but an increased reduced frequency of $k = 0.5$, the wake has some kinks and flow separation emerges towards the bottom of the downstroke. Finally, in Fig. C.22, at the extreme case of $2h_0/c = 0.5$ and $k = 0.5$, massive separation occurs and a leading-edge vortex, visible in positions C and D, convects downstream of the foil.

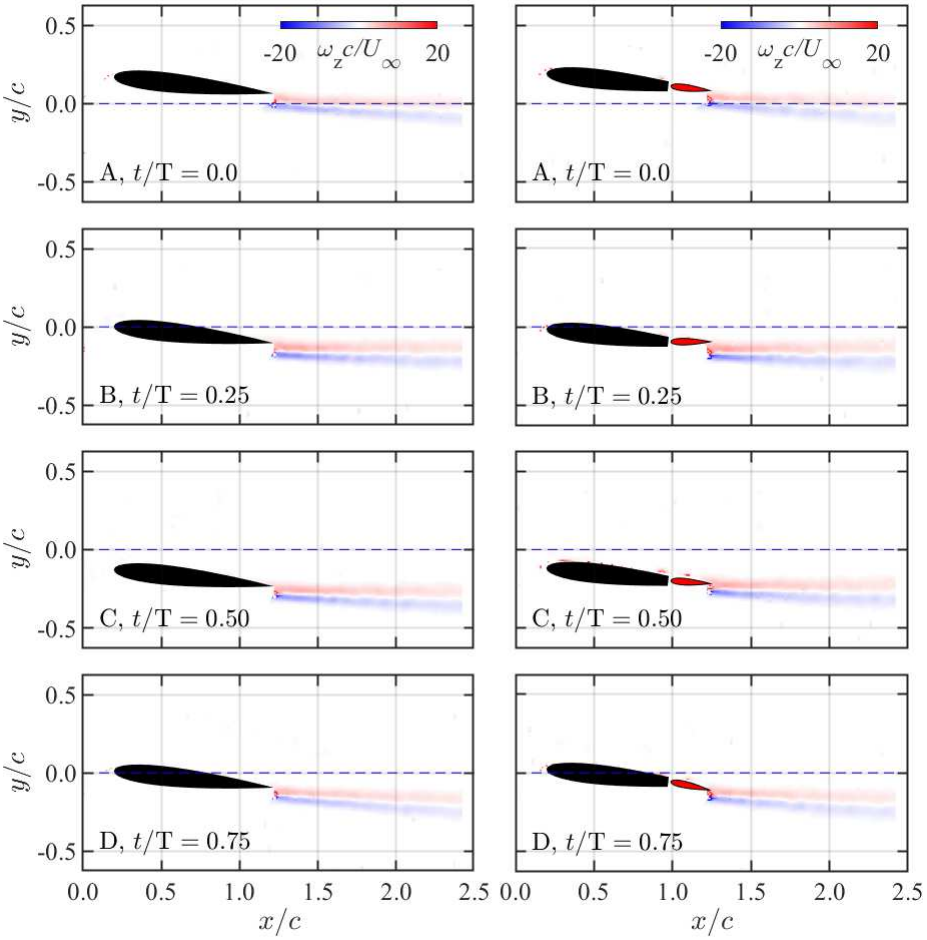

Figure C.19: Vorticity contours at $2h_0/c = 0.3$ and $k = 0.1$

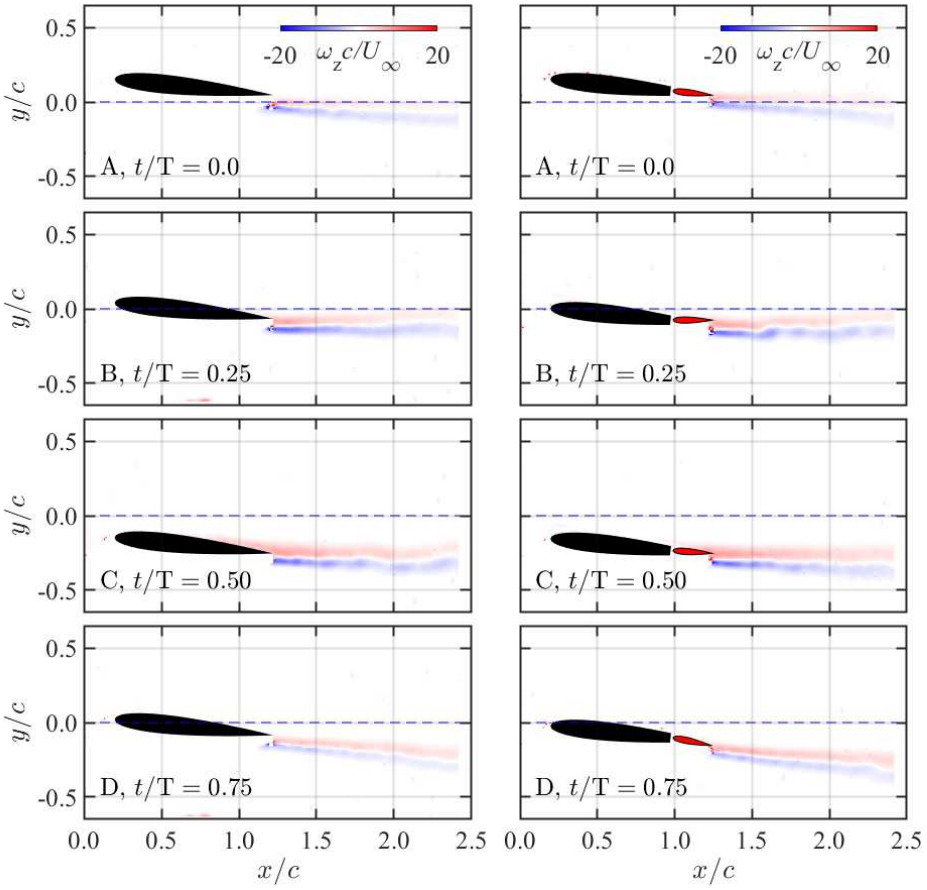

Figure C.20: Vorticity contours at $2h_0/c = 0.3$ and $k = 0.3$

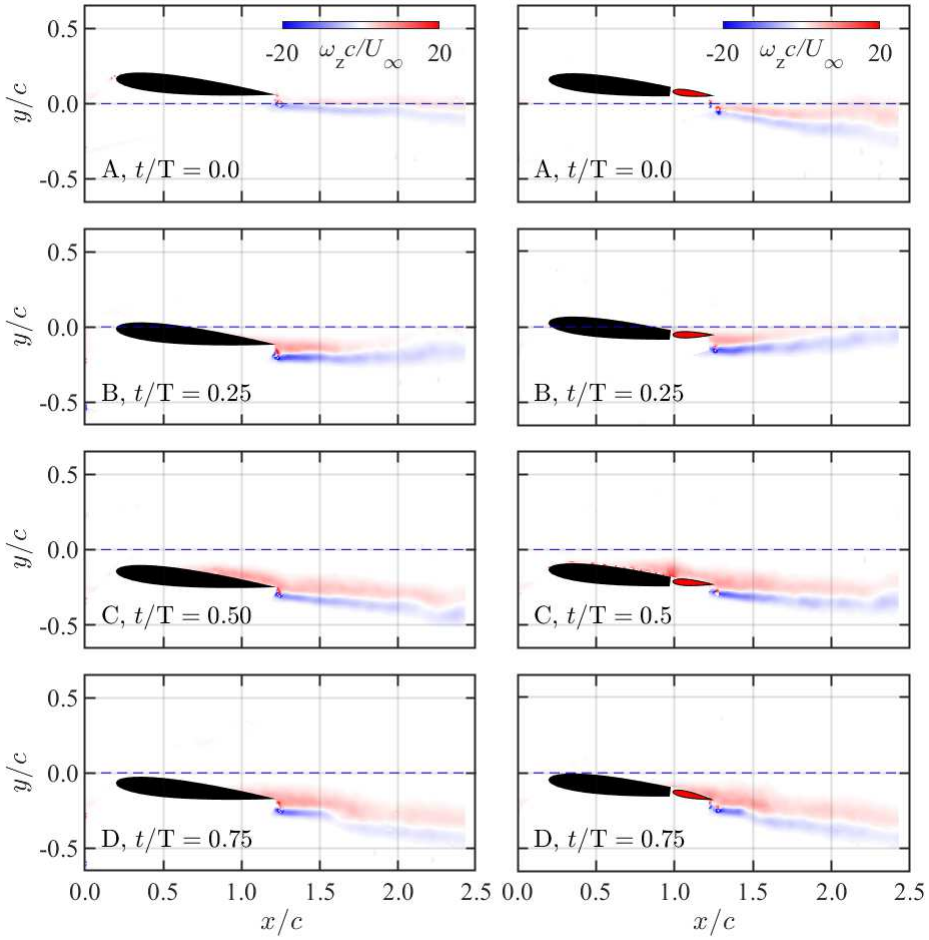

Figure C.21: Vorticity contours at $2h_0/c = 0.3$ and $k = 0.5$

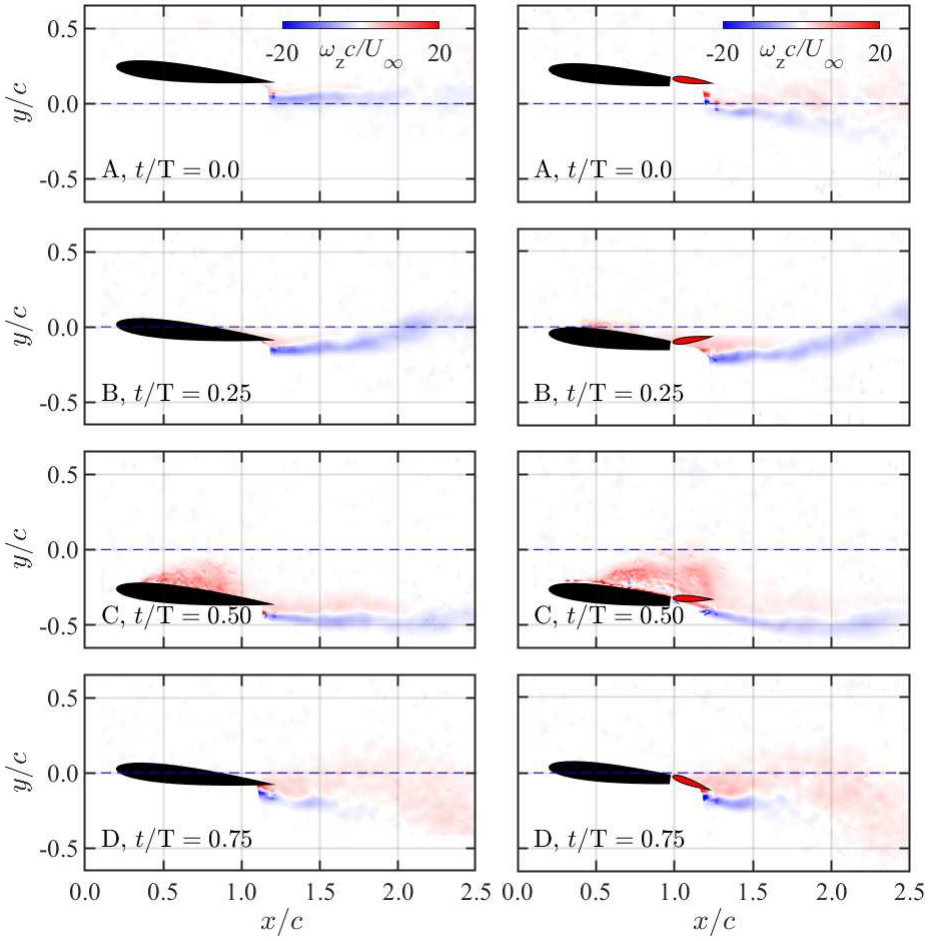

Figure C.22: Vorticity contours at $2h_0/c = 0.5$ and $k = 0.5$.

Appendix D.

Here we consider the effect of a change in the inflow velocity (ΔU) in addition to a change in the incident flow direction ($\delta\alpha$). From Fig. 1(b), the change in angle of attack can be defined as $\Delta\alpha = \delta\alpha - \delta\theta$, where $\delta\alpha$ is the variation on the onset flow direction, while $\Delta\alpha$ is the variation in the angle of attack once the flap is deflected. In this case, a spring deflection $\delta\theta = \delta\alpha$ would account for the change in the angle of attack, but not for the change in velocity. We can quantify $\delta\theta$ by assuming small changes in the flow velocity, by which assumption we can linearise the hydrodynamic pitching moment and consider separately the dependency from the angle of attack and the flow velocity, such that

$$M_{k_s} = -\left(M_h + \Delta\alpha\frac{\partial M_h}{\partial\alpha} + \Delta U\frac{\partial M_h}{\partial U}\right). \tag{D.1}$$

In Eq. D.1, the equilibrium position is achieved when

$$\Delta\alpha\frac{\partial M_h}{\partial\alpha} + \Delta U\frac{\partial M_h}{\partial U} = 0, \tag{D.2}$$

and using $\Delta\alpha = \delta\alpha - \delta\theta$, eq. D.2 can be rearranged as

$$\delta\theta = \delta\alpha + \Delta U\frac{\partial M_h}{\partial U}\left(\frac{\partial M_h}{\partial\alpha}\right)^{-1}. \tag{D.3}$$

The additional deflection due to a change in the flow velocity depends on the increment in the angle of attack $\delta\alpha$, the change in the inflow velocity ΔU and the two hydrodynamic pitching moment partial derivatives. In some applications, however, the effect of ΔU is negligible compared to that of $\delta\alpha$. For example, let us consider a tidal turbine operating in a sheared current, and let us use the flow simulations parameters in Dai et al. [10] at a blade section located at $3/4^{\text{th}}$ of the blade span, for a rotor with hub height of 20 m and a blade length of 9 m,

$$\alpha = 6^\circ, \qquad \delta\alpha = 1^\circ, \qquad U = 7\ \text{m s}^{-1}, \qquad \Delta U = 0.02\ \text{m s}^{-1}, \tag{D.4}$$

here α is the mean angle of attack. We can approximate the leading-edge hydrodynamic pitching moment of a symmetric thin blade below its stall angle as

$$M_h \approx xL \approx \frac{x}{2}\rho U^2 S C_L \approx x\rho U^2 S\pi\alpha, \tag{D.5}$$

where x is the moment arm of the lift force, L is the lift force, ρ is the fluid density, U is the resultant velocity, S is the surface area of the blade and $C_L = 2\pi\alpha$. Taking the partial derivatives of Eq. D.5 with respect to U and α, the second term on the right of Eq. D.3, reduces to $\Delta U(2\alpha/U)$, and the deflection in the blade yields

$$\delta\theta = 1^\circ + 0.034^\circ. \tag{D.6}$$

The first term on the right hand side is the deflection due to $\delta\alpha$, while the second term is that due to ΔU. This result shows that for inflow oscillations due to the ocean shear layer, the dominant effect is that due to $\delta\alpha$. Hence, a highly flexible blade with a constant external moment should cope satisfactorily with narrow band signature marine flow conditions.

References

[1] C. L. Sequeira, R. J. Miller, Unsteady gust response of tidal stream turbines, in: 2014 Oceans - St. John's, 2014, pp. 1–10. doi:10.1109/OCEANS.2014.7003026.

[2] G. T. Scarlett, B. Sellar, T. van den Bremer, I. M. Viola, Unsteady hydrodynamics of a full-scale tidal turbine operating in large wave conditions, Renewable Energy 143 (2019) 199 – 213. doi:https://doi.org/10.1016/j.renene.2019.04.123.

[3] G. T. Scarlett, I. M. Viola, Unsteady hydrodynamics of tidal turbine blades, Renewable Energy 146 (2020) 843 – 855. doi:https://doi.org/10.1016/j.renene.2019.06.153.

[4] R. Nicholls-Lee, S. Turnock, S. Boyd, Application of bend-twist coupled blades for horizontal axis tidal turbines, Renewable Energy 50 (2013) 541 – 550. doi:https://doi.org/10.1016/j.renene.2012.06.043.

[5] K. E. Porter, S. E. Ordonez-Sanchez, R. E. Murray, M. Allmark, C. M. Johnstone, T. O'Doherty, A. Mason-Jones, D. A. Doman, M. J. Pegg, Flume testing of passively adaptive composite tidal turbine blades under combined wave and current loading, Journal of Fluids and Structures 93 (2020) 102825. doi:https://doi.org/10.1016/j.jfluidstructs.2019.102825.

[6] C. G. Anderson, J. B. Richon, T. J. Campbell, An aerodynamic moment-controlled surface for gust load alleviation on wind turbine rotors, IEEE Transactions on Control Systems Technology 6 (5) (1998) 577–595. doi:10.1109/87.709493.

[7] A. Young, J. Farman, R. Miller, Load alleviation technology for extending life in tidal turbines, in: C. Guedes Soares (Ed.), Progress in Renewable Energies Offshore - Proceedings of 2nd International Conference on Renewable Energies Offshore, RENEW 2016, 1st Edition, CRC Press, USA United States, 2016, pp. 521–530.

[8] A. Medina, M. V. Ol, P. Mancini, A. Jones, Revisiting conventional flaps at high deflection rate, AIAA Journal 55 (8) (2017) 2676–2685. doi:10.2514/1.J055754.

[9] P. Mancini, A. Medina, A. R. Jones, Experimental and analytical investigation into lift prediction on large trailing edge flaps, Physics of Fluids 31 (1) (2019) 013106. doi:10.1063/1.5063265.

[10] W. Dai, G. Pisetta, I. M. Viola, Morphing blades for passive load control of tidal turbines, in: EWTEC 2019.

[11] G. He, J. Deparday, L. Siegel, A. Henning, K. Mulleners, Stall delay and leading-edge suction for a pitching airfoil with trailing-edge flap, AIAA Journal Articles in Advance (2020) 1–10. doi:10.2514/1.J059719.

[12] T. Theodorsen, General theory of aerodynamic instability and the mechanism of flutter, NACA Technical Report No. 496.

[13] J. G. Leishman, Principles of helicopter aerodynamics, 2002.

[14] C. Tropea, A. Yarin, J. Foss, Springer Handbook of Experimental Fluid Dynamics, Springer, Heidelberg., 2007.

[15] R. E. Sheldahl, P. C. Klimas, Aerodynamic characteristics of seven symmetrical airfoil sections through 180-degree angle of attack for use in aerodynamic analysis of vertical axis wind turbines, Sandia National Laboratories.doi:10.2172/6548367.

[16] L. Mendelson, A. H. Techet, Quantitative wake analysis of a freely swimming fish using 3D synthetic aperture PIV, Experiments in Fluids 56 (7) (2015) 135. doi:10.1007/s00348-015-2003-x.

[17] G. Z. McGowan, K. Granlund, M. V. Ol, A. Gopalarathnam, J. R. Edwards, Investigations of Lift-Based Pitch-Plunge Equivalence for Airfoils at Low Reynolds Numbers, AIAA Journal 49 (7) (2011) 1511–1524. doi:10.2514/1.J050924.

[18] A. M. Young, A. S. Smyth, Gust–airfoil coupling with a loaded airfoil, AIAA Journal 59 (3) (2021) 773–785.

[19] H. J. Bird, S. Otomo, K. K. Ramesh, I. M. Viola, A geometrically non-linear time-domain unsteady lifting-line theory, in: AIAA Scitech 2019 Forum. doi:10.2514/6.2019-1377.

[20] H. J. Bird, S. Otomo, K. K. Ramesh, I. M. Viola, Applying inviscid linear unsteady lifting-line theory to viscous large-amplitude problems, arXiv e-prints.

[21] L. Graftieaux, M. Michard, N. Grosjean, Combining PIV, POD and vortex identification algorithms for the study of unsteady turbulent swirling flows, Meas Sci Technol 12 (1201) (2001) 1422–1429. doi:10.1088/0957-0233/12/9/307.

[22] C. E. Morgan, H. Babinsky, J. K. Harvey, Vortex detection methods for use with PIV and CFD data, in: Proceedings of the 47th AIAA Aerospace Sciences Meeting, Orlando, Florida, USA, 2009. doi:10.2514/6.2009-74.

[23] A. Arredondo-Galeana, I. M. Viola, The leading-edge vortex of yacht sails, Ocean Engineeringdoi:10.1016/j.oceaneng.2018.02.029.